Description and dosimetric verification of the PEREGRINE Monte Carlo dose calculation system for photon beams incident on a water phantom

C. L. Hartmann Siantar,[a] R. S. Walling, and T. P. Daly
Lawrence Livermore National Laboratory, Livermore, California 94550

B. Faddegon and N. Albright
Department of Radiation Oncology, University of California San Francisco, San Francisco, California 94143-1708

Paul Bergstrom
Lawrence Livermore National Laboratory, Livermore, California 94550

A. F. Bielajew
University of Michigan

C. Chuang
Department of Radiation Oncology, University of California San Francisco, San Francisco, California 94143-1708

D. Garrett, R. K. House, and D. Knapp
Lawrence Livermore National Laboratory, Livermore, California 94550

D. J. Wieczorek and L. J. Verhey
Department of Radiation Oncology, University of California San Francisco, San Francisco, California 94143-1708

(Received 18 October 2000; accepted for publication 8 May 2001)

PEREGRINE is a three-dimensional Monte Carlo dose calculation system written specifically for radiotherapy. This paper describes the implementation and overall dosimetric accuracy of PEREGRINE physics algorithms, beam model, and beam commissioning procedure. Particle-interaction data, tracking geometries, scoring, variance reduction, and statistical analysis are described. The BEAM code system is used to model the treatment-independent accelerator head, resulting in the identification of primary and scattered photon sources and an electron contaminant source. The magnitude of the electron source is increased to improve agreement with measurements in the buildup region in the largest fields. Published measurements provide an estimate of backscatter on monitor chamber response. Commissioning consists of selecting the electron beam energy, determining the scale factor that defines dose per monitor unit, and describing treatment-dependent beam modifiers. We compare calculations with measurements in a water phantom for open fields, wedges, blocks, and a multileaf collimator for 6 and 18 MV Varian Clinac 2100C photon beams. All calculations are reported as dose per monitor unit. Aside from backscatter estimates, no additional, field-specific normalization is included in comparisons with measurements. Maximum discrepancies were less than either 2% of the maximum dose or 1.2 mm in isodose position for all field sizes and beam modifiers. [DOI: 10.1118/1.1381551]

Key words: Monte Carlo, radiation therapy, treatment planning, dose calculation

I. INTRODUCTION

Dose calculation accuracy is a critical part of radiation therapy. Combining first-principles physics with physical descriptions of the radiation source and patient, Monte Carlo transport methods have the potential to calculate dose accurately over a wide variety of treatment delivery and patient conditions.[1–8] Owing to development of faster codes designed specifically for dose calculation in radiotherapy[9–15] and rapidly increasing computer speeds, it is now possible to use three-dimensional (3D) Monte Carlo methods for day-to-day treatment planning.

Accurate dose calculation requires accurate characterization of the radiation source. This can be accomplished with high fidelity and exceptional detail by simulating the transport of particles through the accelerator head and beam delivery system.[16–22] Recent work has described accelerator simulations in a two-step process.[6,23,24] First, an initial Monte Carlo simulation of the accelerator head is done to produce a file containing the phase space for a large ensemble of representative particles. Then, the phase space file is condensed into a photon beam model, i.e., a set of probability distributions which can be sampled to obtain particles for transport through the treatment-dependent parts of the beam delivery system. Simulations are based on generic manufacturer descriptions, and can include assumptions about initial electron beam characteristics (energy, spot size, divergence, etc.). A

Monte Carlo treatment planning calculation system must account for the details of each individual accelerator, including beam tuning, to provide accurate dose calculations.[25]

This work summarizes the PEREGRINE system,[11] its x-ray beam model, and commissioning procedure. (Some of the features described in this article are available as a commercial product from NOMOS Corporation, Sewickley, PA.) A method of determining the beam representation, or instantiation, is demonstrated for a specific accelerator. Studies investigating the accuracy of photon beam simulations fall into two general categories: validation that beam models accurately reproduce characteristics of the initial phase space generated by Monte Carlo methods[23,26] and experimental verification of dose distributions in a phantom. The x-ray beam model used in PEREGRINE has already been shown to faithfully reconstruct the phase space.[23] In this paper, we investigate the accuracy of its dose predictions for x-ray therapy, describing a set of experimental comparisons for 6 and 18 MV x-ray beams (Varian Clinac 2100C accelerator) incident on a water phantom. Open field comparisons are made for field sizes ranging from 2×2 to $38\times38\,\mathrm{cm}^2$. We also compare calculations with measurements for fields modified by representative wedges, a block, and multileaf collimator.

II. MATERIALS AND METHODS

The first part of this section describes the implementation of Monte Carlo transport methods, a beam model, and a beam commissioning procedure for the PEREGRINE system. In Sec. II A we describe the particle–interaction processes (physics), transport methods, tracking geometries, scoring, variance reduction, and statistical analysis methods used for this study.

The beam model consists of a set of photon sources representing target, flattener, and primary collimator, and a single extended electron source. Published measurements provide an estimate of backscatter on monitor chamber response. The magnitude of the electron source is increased to improve agreement with measurements in the buildup region.

Commissioning consists of three steps: (1) selecting the electron beam energy, (2) determining the scale factor that defines dose per monitor unit, and (3) describing treatment-dependent beam modifiers. To select the electron beam energy, we use dose calculations made from full treatment head simulations at discrete electron energies to calculate off-axis ratios (OARs) for a $38\times38\,\mathrm{cm}^2$ field at 10 cm depth. By comparing these OARs with measurements, we choose an intermediate beam energy which gives the best match. Representations of the beam model, precalculated from the phase space data, are then interpolated to this energy. The calibration scale factor is set according to the Gy-to-MU calibration condition of the specific accelerator. Finally, collimator jaws, wedges, wedge trays, block trays, and multileaf collimators (MLCs) are described in terms of density, composition, shape, and location. The thickness, material, density, and aperture shape for a block and leaf positions for a MLC are described by the user at calculation time.

In Sec. II D, we provide a description of the measurements used for dosimetric comparisons shown in Sec. III. These include accelerator, detector, and water phantom characteristics.

A. Monte Carlo code description

Monte Carlo particle (history) simulations follow a three-step transport process. First, a particle is selected from the radiation source, described as a set of energy, angular, and position distributions derived from a particle phase-space file. The beam model is described in more detail in Sec. II B. The particle is then tracked through the treatment-specific beam delivery components (collimator jaws, wedges, blocks, multileaf collimator, etc.) and the air column until it reaches the boundary of the Cartesian grid that defines the patient (patient mesh). Finally, the particle is tracked through the patient mesh (built from a CT scan), recording dose deposition, defined as energy/mass in collection volume, on a user-specified grid. At each point of interaction, the phase space (energy, trajectory, and position) descriptions for secondary photons, electrons, and positrons are stored in a set of arrays, which are emptied before a new source particle is selected. This process continues for millions of histories, until the user-specified stopping condition (number of histories or statistical figure of merit) is met.

Source, transport, and collection modules are programmed in FORTRAN, while I/O and parallel-processing software is programmed in C. Parallel processing software uses POSIX threads, which are available on most operating systems. PEREGRINE is designed to operate on a variety of UNIX operating systems, but is usually operated on the Solaris operating system.

1. Physics

a. Photons. PEREGRINE determines the total cross section for the photon interacting in the medium from the sum of the cross sections for Compton scattering, the photoelectric effect, pair and triplet production, and Rayleigh scattering. Total cross sections are taken from the Evaluated Photon Data Library.[27] Compton scattering is treated in the incoherent scattering factor approximation.[27,28] This approximation modifies the Klein–Nishina picture of Compton scattering to incorporate atomic binding effects. The photoelectric effect electron is assumed to be ejected from the K shell of the atom with a direction determined from Sauter's K shell formula.[29] The binding energy of the photoelectron is deposited at the point of interaction. Pair production cross sections include both production of pairs in the field of the nucleus and their production in the field of the atomic electrons (triplet production).[27,30] Cross sections for these processes are added and treated as pair production in the field of the nucleus. The energy sharing between the electron and the positron is determined by the Bethe–Heitler formula. Rayleigh scattering is treated in the form factor approximation.[27,28]

b. Charged particles. PEREGRINE uses unrestricted stopping powers calculated from the formulas described in ICRU Report 37.[31] The stopping powers that the code produces are in agreement with those tabulations. The density effect correction to the stopping power is calculated using a standard, prespecified material density. If PEREGRINE uses the material at a nonstandard density in the simulation, it does not recalculate the density effect correction. As a simplification, PEREGRINE uses electron total stopping powers for both electrons and positrons. For electron energies between 0.1 and 100 MeV, the stopping powers of electrons and positrons differ by less than 6% for elements ranging from carbon to lead.[32] The difference in stopping powers is larger for energies below 0.1 MeV, but ranges of these particles are less than 1 mm at typical tissue densities. For the most energetic photon beam used in this study (18 MV), 9% of the dose in a water phantom can arise from positrons. This results in a $<0.5\%$ error in dose, which is likely to be small compared to other uncertainties. PEREGRINE transports electrons using class II condensed history methods (see Sec. II A 2), and precalculates restricted collisional and radiative stopping powers, to avoid double-counting processes that are handled on an event-by-even basis. Restricted collisional stopping powers are determined as described in ICRU 37, to subtract above-threshold Møller (electrons) and Bhabha (positrons) scattering processes from collisional stopping powers. Restricted radiative stopping powers are determined by subtracting a numerical integration of the above-threshold bremsstrahlung processes from the radiative stopping power.

The implementation for sampling knock-on events of Møller scattering (for electrons) and Bhabha scattering (for positrons) is the same as for the EGS4 code,[33] but modified by a correction that repaired an error in the EGS4 code related to the rare sampling of high-energy knock on electrons.[34] The bremsstrahlung cross sections and emitted photon spectral data were obtained from the Lawrence Livermore National Laboratory's Evaluated Electron Data Library.[35] For each bremsstrahlung event, the bremsstrahlung photon energy is subtracted from the primary electron energy. The angle of the emitted bremsstrahlung photon is determined from a simplification of a method described and evaluated elsewhere.[36,37] The primary electron is not deflected after a bremsstrahlung event.

2. Transport methods

PEREGRINE has two sets of particle tracking algorithms, one for the beam delivery system and the other for the patient.

a. Photons. In the beam delivery system, photons are tracked using standard analog methods: Given a particle energy, location, and trajectory, calculate the distance to the zone boundary and the next collision; move particle to the minimum of these distances; if the minimum distance is to a collision, determine energy and angle of all daughter products. In this study, the minimum photon tracking energy in the beam delivery system was 10 keV.

In the patient, photons are tracked through the CT scan-derived transport mesh using the delta scattering method.[38] This allows PEREGRINE to avoid computationally expensive distance-to-boundary calculations without biasing the resulting dose calculations. The delta scattering method selects a tentative collision site as if the patient mesh were uniformly filled with material of cross section equal to the maximum cross section at the photon energy of any material in the patient mesh. It then accepts a tentative collision as being real with probability equal to the ratio of the actual cross section at the tentative collision site to the maximum cross section. If the collision is real, the photon obtains a new energy and direction. If the collision is not real, the photon keeps its original energy and direction. It then repeats the process to calculate the next tentative collision site. In this study, the minimum photon tracking energy in the patient was 100 eV.

b. Charged particles. PEREGRINE uses the class-II condensed history method for charged particle transport,[39] modeling knock-on and bremsstrahlung processes above specified cutoff energies as discrete events. The Molière[40] method, implemented as in the EGS4 code, is employed to account for multiple scattering. The condensed history electron step size taken is determined by the minimum of the step size necessary to create a bremsstrahlung photon, to generate a knock-on electron, to reach the next spatial boundary, to reach the next energy bin boundary, or $S_{\max}$. $S_{\max}$ is always 1 mm in the patient. In the beam delivery system, $S_{\max}$ is 1 cm for steps in air and 1 mm in all other materials. PEREGRINE divides the energy axis of the electrons into bins, the boundaries of which are a logarithmic scale of round numbers, namely: 1, 1.25, 1.5, 1.75, 2, 2.5, 3, 3.5, 4, 4.5, 5, 5.5, 6, 7, 8, 9 in each decade. The particle's current energy bin number is used for table lookup and decision making. Terminating the electron step at each energy bin boundary ensures that the fractional energy loss in a step never exceeds 20%. The electron step is typically broken into two substeps by deflecting the particle by the multiple scattering angle for the full step at a random point along the step, following the random hinge method developed for the PENELOPE Monte Carlo code.[41] The random hinge method takes into account the curvature of the electron step as well its lateral deflection. The quality of this random hinge has been analyzed by Kawrakow and Bielajew[42] through demonstration of the close agreement with the exact Lewis moments, the average lateral and longitudinal displacements.[43] In the patient mesh, energy is deposited at a random location along each substep. This is necessary because the dose-scoring grid is independent of the transport grid, as described in the following. Since the EGS4-based Moliére multiple scattering method is employed, the multiple scattering angle predicted for a 1 mm ($S_{\max}$ in the patient) path length in air cannot be modeled accurately because the path length is too short.[40] Despite this shortcoming, accurate dose prediction is not compromised in this application, as the EGS4 code has been applied successfully in similar but more demanding applications, e.g., ionization chamber simulations with air cavity size on the order of mm.[44]

In the beam delivery system, electrons can be tracked

with different levels of approximation, depending on the beam modifier and user-defined tracking and cutoff options. We used the following options for this work: 10 keV bremsstrahlung creation threshold, 100 keV kinetic energy knock-on electron creation threshold, and 100 keV kinetic energy electron tracking cutoff. In this paper, we use fewer approximations in the beam delivery system than recommended in a recent publication[45] in order to minimize their impact on comparisons with measurements.

In the patient mesh, termination of the electron trajectory is determined by its kinetic energy and its location in the geometry. The track terminates when the electron's energy falls below the energy required to traverse one-third of the voxel's minimum dimension (approximately 180 keV kinetic energy for 1 mm voxels in water). Electrons are never transported below 10 keV kinetic energy. Once the particle reaches the minimum tracking energy, its residual energy is deposited at a random location along a straight-line trajectory of length equivalent to its residual range. The termination of a positron trajectory results in the emission of two 511 keV annihilation photons. The creation thresholds for bremsstrahlung and knock-on electrons were set at 10 and 100 keV kinetic energy, respectively, in the patient mesh.

3. Geometry

Beam modifiers are described as collections of six-sided prisms, with boundaries defined by the physical dimensions of the modifier. Collimator jaws can move along a line or arc, matching their physical implementation in the accelerator treatment head. Aperture blocks are modeled as a diverging raster of voxel prisms with lateral dimensions defined by the user. In multileaf collimators, the convex leaf ends (Varian design) and tongue-and-groove features are modeled explicitly. Wedges are defined as a series of contiguous trapezoidal prisms. All block and wedge trays are modeled as uniform slabs of material, with lateral extents corresponding to their physical dimensions. All space not occupied by solid, beam-modifying material is filled with air, in which particles are allowed to interact. The user assigns all beam-modifier materials and densities in the device description input file.

The patient mesh is taken directly from the CT scan, with no reduction in resolution. The user assigns material to each voxel by specifying predefined materials for ranges of CT number. The user specifies density from the CT number with a monotonically increasing, piecewise-continuous linear function. Each material can also be defined with a default density. In this study, we assign only unit-density water to each CT element, as this is the only material used for experiments shown.

4. Scoring

Dose is scored on a grid that is independent from the CT-derived Cartesian grid that is used for particle transport. This permits PEREGRINE to speed up the calculation by using variance reduction techniques in regions that lie outside of the dose-scoring grid, and provides the user with flexibility in assigning dose-grid resolution.

Dose is scored in a set of spheres that are centered on the points of a grid with cubical unit cells. The spheres, referred to as dosels, are configured to touch along cube diagonals and overlap elsewhere. The transport algorithms in PEREGRINE deposit energy at a random point along the electron step, as opposed to depositing energy inside a given CT voxel. When energy is deposited at a point in space, the energy is added to every sphere that contains that point. To obtain dose, the energy is divided by the mass of the sphere, which is determined in a setup calculation that utilizes a closed form solution for the common volume of a sphere and a rectangular parallelepiped. Spheres were selected as a way of approximating the dose reported at a point for a region of nonuniform density. The spheres have a larger volume than the cube defined by the grid points. This causes the calculation to reach a given statistical noise level faster than it would if the dose were collected in the cubes. Although overlapping spheres cause neighboring points to be correlated, they provide slightly higher resolution than would be obtained with dose collection elements of the same volume that do not overlap.

In this study, the separation of the dosel center points was 2 mm for each case other than two largest open fields. The $38\times38\,\mathrm{cm}^2$ field used a separation of 4 mm and the $20\times20\,\mathrm{cm}^2$ used a separation of 3 mm. The voxels describing the uniform water phantom were $1\times1\times20\,\mathrm{mm}^3$. In general, we use a dosel grid spacing that is larger than the minimum voxel dimension.

5. Variance reduction

Several variance reduction techniques are used in PEREGRINE: source particle reuse, range rejection, and splitting/Russian rouletting.

a. Source particle reuse. Each source particle that survives transport through the modifiers is reused a fixed number of times. Photons are reused upon entering the CT grid. Electrons are reused upon entering the air column below the last modifier. Electrons are treated differently from photons because electrons interact in every voxel that they cross. When electrons are reused upon entering the CT grid, each of the reused electrons tends to deposit a similar amount of energy in the first voxel it crosses. This causes the dose at the edge of the CT grid to be noticeably noisier than the rest of the dose distribution since it arises from fewer independent depositions. Reusing the electrons at the bottom of the last modifier permits the electrons to spread out before entering the CT grid and eliminates the noisy dose at the edge of the CT grid.

Various considerations limit the number of times that the source particles should be reused. Source particle reuse should not be increased beyond the point at which the fraction of the total computer time spent in bringing the particles to the CT grid becomes small, or to the point that ranges of the electrons created by different reused photons greatly overlap. This lowers the independence of the depositions and may increase the amount of computer time needed to make the spatial distribution of the dose become smooth. The num-

ber of times that source particles can be reused is also limited by the requirement that the source be adequately sampled during the course of the run. In this study, source particles were reused 10 times.

b. Range rejection. An electron with a continuous slowing-down approximation range that is less than 1/3 the smallest dimension of a CT voxel is terminated and its energy is dumped at a random point along a straight line of length equal to its residual range. The 1/3-of-range criterion was the largest value that eliminated boundary artifacts in dose, in investigations where dose was tallied on the voxel grid. The 1/3 criterion is applied to voxels, as they are always smaller than dosels, making them the conservative choice for limiting range. In a setup calculation, each voxel is assigned a range rejection energy using this criterion. Electrons are never transported below 10 keV, regardless of the range rejection energy.

Implementing range rejection for a 6 MV water phantom case with voxels of minimum dimension equal to 1 mm lowered the computer time required to achieve a given statistical error by a factor of 0.6. With range rejection, electrons were tracked down to 175 keV and without it they were tracked down to 10 keV.

c. Russian rouletting and splitting. For this study, photons that are outside the dose-scoring region and are moving away from the dose scoring region were Russian rouletted with a probability of 1/10. If descendents of rouletted photons move toward or enter the dose-scoring region, they were split into triplets. The number of times that roulletting and splitting can happen to the descendents of a photon is limited to avoid the generation of very high and very low weight particles.

Implementing on Russian rouletting for a 6 MV $38 \times 38\,\mathrm{cm}^2$ field lowered the computer time required to achieve a given statistical error by a factor of 0.6. The dose collection grid in this case consisted of a single string of dosels along the beam axis. The separation between the centers of the dosels on the string was 4 mm.

6. Statistical analysis

The Monte Carlo calculation is considered to have converged to a fractional error, F, when the standard deviation of the dose of every dosel is less than $F*M_d$, where M_d is the largest dose in any dosel. Calculating the standard deviation in every dosel results in a significant expenditure of memory and time due to the large size of the dosel array. For this reason, we provide a statistical figure of merit based only on the standard deviation calculated for a single dosel, which we refer to as the watch dosel. The watch dosel is selected during the first part of the run as the dosel with the maximum dose after a fixed number of histories, H. H is chosen to be large enough that the watch dosel will, at the end of the run, have a dose that is close to M_d. The run is terminated when the standard deviation of the watch dosel is less than $F*W_d$, where W_d is the dose in the watch dosel. For the results shown in this study, the value of $F=0.005$ was used. The standard deviation of the watch dosel was calculated from batch averages using a recursion relationship similar to that described in Ref. 46. There are typically thousands of batches in a run.

For dosels with similar density, the variance in a PEREGRINE calculation tends to be proportional to the dose. If the variance were exactly proportional to the dose for every dosel in the problem, then the dosel with the maximum dose would also be the dosel with the maximum standard deviation. If this were true, the termination criterion based on the standard deviation of the watch dosel would be equivalent to the termination criterion based on the standard deviation of every dosel.

The standard deviation that goes with a given dose tends to decrease as the density of the dosel increases. For this reason, the watch dosel is selected from dosels that have a mass that is between one-fourth and three times the mass of a water dosel.

B. Source description

The non-patient-specific parts of the Varian high energy family of accelerators (Clinacs 2100C, 2100C/D, 2300C/D) are simulated for 6 and 18 MV using the BEAM Monte Carlo code.[18] The physical dimensions and materials of the accelerator were obtained from the manufacturer (Varian Oncology Systems, Palo Alto, CA).

1. BEAM simulations

The BEAM simulation used here extends from the top of the bremsstrahlung target to the bottom of the monitor chamber. The electron beam incident on the target was assumed to have no divergence, to be monoenergetic, and to have a uniform spatial distribution with 1 mm radius. The delta ray and bremsstrahlung production cutoffs were taken to be AE $=521\,\mathrm{keV}$ (kinetic+rest mass) and AP$=10\,\mathrm{keV}$. The electron and photon transport cutoffs were taken to be ECUT $=611\,\mathrm{keV}$ (kinetic+rest mass) and PCUT$=100\,\mathrm{keV}$. We used the variance reduction technique of splitting every bremsstrahlung photon into 20 photons, and employed the PRESTA[47] electron step algorithm. The number of histories for each case was chosen to produce phase space files containing about 30 m particles.

2. BEAM model

The phase space file resulting from the BEAM simulation is used to generate a set of histograms that can be sampled to approximately recreate the phase-space characteristics of the particles described in the file.

These histograms form a part of the PEREGRINE device file, which characterizes the accelerator according to the beam model, described elsewhere.[23] During a PEREGRINE calculation, the histograms are sampled to generate the particles that are then tracked through treatment-specific beam modifiers (collimator jaws, wedge, block, multileaf collimator, etc.) and the patient.

Particles in the phase space file are divided into four subsources depending on the location of their last interaction, which is determined by the LATCH variable in BEAM:

Subsource 1: photons for which the target is the last interaction.

Subsource 2: photons for which the primary collimator is the last interaction.

Subsource 3: photons for which the flattening filter is the last interaction.

Subsource 4: all electrons.

To calculate histograms for each subsource, particles are projected in straight lines (assume no collisions, no collimator jaws, etc.) from the bottom of the monitor unit chamber, which is the location of the BEAM phase space file, to the isocenter plane, which is defined to be 100 cm from the target. Particles that strike the isocenter plane at the larger values of radius are left out of the device file histograms, with the assumption that they are blocked by the jaws at the widest field setting. For each subsource, R_{max} is calculated as an estimate of the maximum radius illuminated in the isocenter plane by that subsource when the jaws are set to a $40\times 40\,cm^2$ field. This radius lies in the corner of the square field. Phase space particles that cross the isocenter plane beyond R_{max} are not included in the device file histograms. For the accelerators modeled in this study, R_{max} was about 30 cm for subsources 1 and 2, and about 50 cm for subsources 3 and 4. R_{max} includes nearly all the photons from phase space file for subsource 1. For subsources 2, 3, 4, the planar energy fluences on the isocenter plane from the phase space file are strongly clipped by R_{max}, at greater than the 15% of maximum level. A histogram of the rotationally symmetric planar energy fluence in the isocenter plane is calculated for each subsource extending to R_{max} and entered in the device file.

The method used to calculate R_{max} for photons does not work as well for the contaminant electron subsource since electrons do not travel in straight lines in the air. Values of R_{max} for electrons are checked to ensure that the simulated dose in the build up region of water phantoms is not appreciably affected by increasing R_{max}.

The total energy crossing the isocenter plane inside of R_{max} for each subsource is calculated from the phase space file. These four values are then normalized to give the fractional energy of each subsource.

For each subsource, the isocenter plane out to R_{max} is divided into a set of annular tiles of equal width. A set of histograms is calculated for the particles belonging to each tile of each subsource. These histograms are calculated under the assumption that the phase space file is rotationally symmetric. If it is not, the histograms will still be rotationally symmetric.

Histograms describing the energy spectrum and the directional spectrum are calculated for each tile of each subsource. The energy and directional spectra for particles in a given tile are assumed to be independent. The propagation direction of a particle is specified by its intersection with two planes, the isocenter plane and the virtual source plane, VSP. The VSP is defined as follows (see Fig. 1). Vectors describing the particles in each tile, when projected back along their trajectory, converge to a minimum radius, or bottleneck, close to the central axis of the beam near the point of their last scattering. For example, particles in the flattening filter

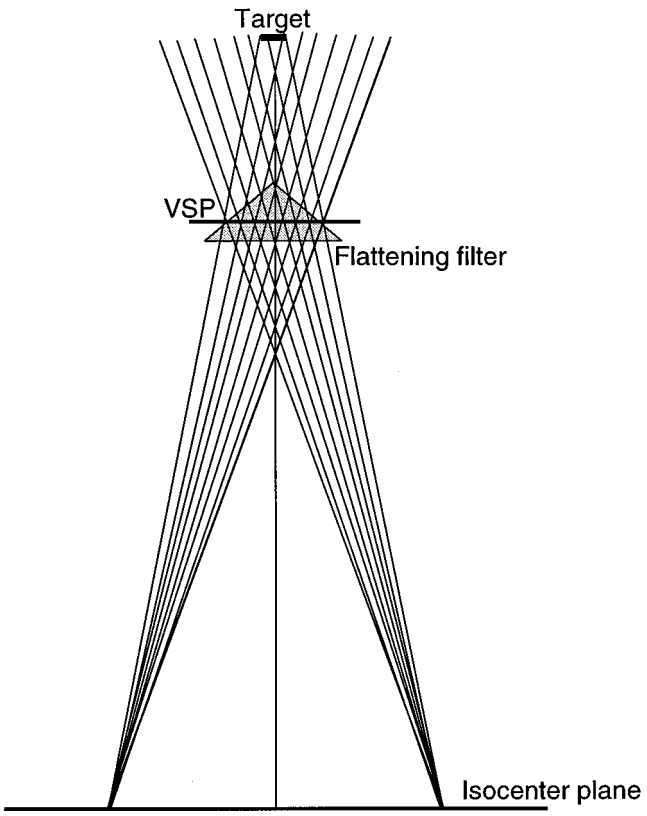

FIG. 1. The trajectories of particles that scatter from the flattening filter and cross the isocenter plane in a given tile form an hourglass figure with a neck close to the flattening filter.

subsource form a bottleneck close to the location of the flattening filter. A plane perpendicular to the beam axis, called the VSP, is selected close to the bottleneck. The planar energy fluence in the VSP associated with particles that cross the isocenter plane in a given tile is a function of the polar

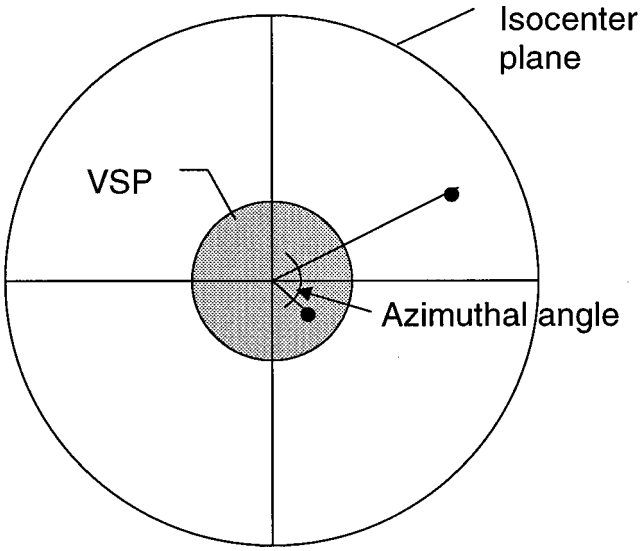

FIG. 2. Beams eye view of the azimuthal angle. The black dots are the intercepts of the particle in the isocenter plane and in the VSP. The azimuthal angle is the angle between the two radial lines.

coordinates about the beam axis, namely the radius and the azimuthal angle (see Fig. 2). The azimuthal angle is the angle lying in the VSP between the intersection of the particle with the VSP and the plane containing the central axis of the beam and the intersection of the particle with the isocenter plane. If one rotates the particle intersection in the isocenter plane about the beam axis, then the corresponding distribution in the VSP also rotates. The planar energy fluence in the VSP is assumed to be separable in radius and azimuthal angle. The exact location of the VSP is automatically adjusted to make this a good approximation. Radial and azimuthal angle histograms of the planar energy fluence in the VSP are calculated for each tile.

The PEREGRINE device file then contains the following information derived from the BEAM simulation

(1) The radial dependence of the rotationally symmetric planar energy fluence in the isocenter plane for each subsource.
(2) The energy spectrum for each tile of each subsource.
(3) The radial and azimuthal angle components of the planar energy fluence in the VSP for each tile of each subsource.
(4) The fraction of the energy contained in each subsource.

The device file also contains a factor that converts monitor units into dose in water, consistent with the calibration of the specific accelerator being simulated, a description of the beam modifiers (material, density, and dimensions), and coefficients that are used to correct for backscatter into the monitor unit chamber as a function of jaw opening (this correction is required since PEREGRINE does not simulate backscatter into the monitor unit chamber).

The device file contains the planar energy fluence on the isocenter plane rather than the planar particle fluence, and the fraction of the energy rather than the fraction of the particles in each subsource. Because energy-based quantities are more closely related to the dose than number-based quantities, sampling from these distributions makes the device file easier to interpret and reduces the likelihood of artifacts resulting from improper binning of rapidly varying energy and particle fluence distributions.

Histograms from the device file are sampled during a PEREGRINE simulation as follows.

(1) A particle is selected from one of the four subsources with a probability equal to the fractional energy in the subsource. The particle weight is adjusted to compensate having sampled fractional energy instead of fractional particle number.
(2) The (x,y) location in the isocenter plane is uniformly sampled, with particle weight modified to account for planar energy fluence.
(3) The tile is randomly selected to be one of the two tiles with center of annulus closest to (x,y). This is equivalent to smoothly interpolating the tile probability distributions with the distance from the axis in the isocenter plane.

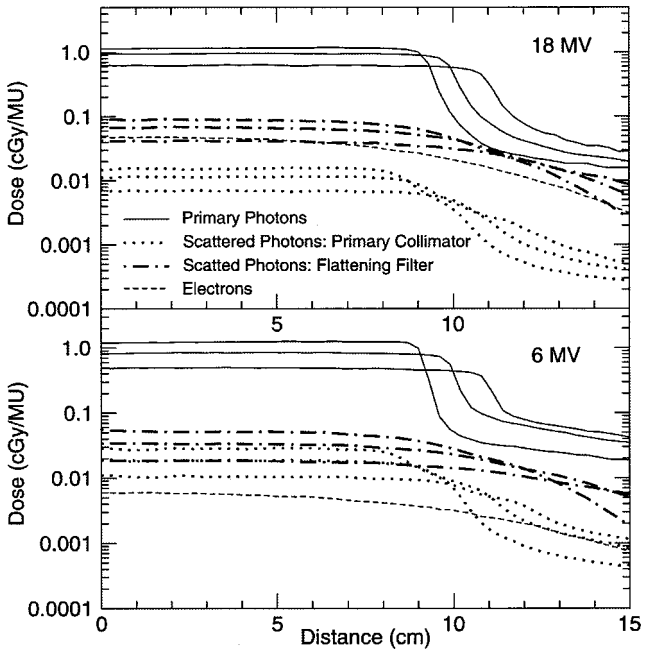

FIG. 3. Dose profiles at d_{max} (1.5 and 3.2 cm for 6 and 18 MV, respectively), 10, and 20 cm depths for $20\times20\ cm^2$ 6 and 18 MV beams incident on a water phantom, positioned at 90 cm SSD. Curves show the effect of primary photon, scattered photon, and electron subsources on calculated profiles. The single electron subsource curve shown here corresponds to the calculated profile at d_{max}.

(4) The energy of the particle is sampled from an energy spectrum of the tile.
(5) The intersection of the particle trajectory in the virtual source plane is sampled by treating the virtual source plane energy fluence as a probability distribution. The trajectory of the particle is determined by connecting the points in the virtual source plane and the isocenter plane.

Figures 3 and 4 show the magnitude and distribution of the dose resulting from individual subsources for a $20\times20\ cm^2$ field incident on a water phantom positioned at 90 cm source-to-surface distance (SSD). Profiles were taken at the nominal depth of maximum dose, d_{max} (1.5 cm at 6 MV, 3.2 cm at 18 MV), 10, and 20 cm. The primary photon subsource provides the largest contribution to dose, followed by the scattered-photon subsource associated with the flattening filter. Scattered photon subsources have depth-dose characteristics similar to the primary photon source. Depth-dose distributions in Fig. 4 show the electron subsource contributing significantly to the dose for 6 and 18 MV beams, from the surface down through d_{max}. Scattered photon and contaminant electron subsources play an increasingly important role for increasing field size.

Because PEREGRINE does not account for particles scattered back into the treatment head, a measurement-based method is used to estimate the effect of backscatter on the over-response of the monitor chamber. While backscatter factor measurements have been reported by several authors, (Ref. 48, for example) we used measured backscatter factors reported by Ref. 49, as these fit our data the best. Backscatter

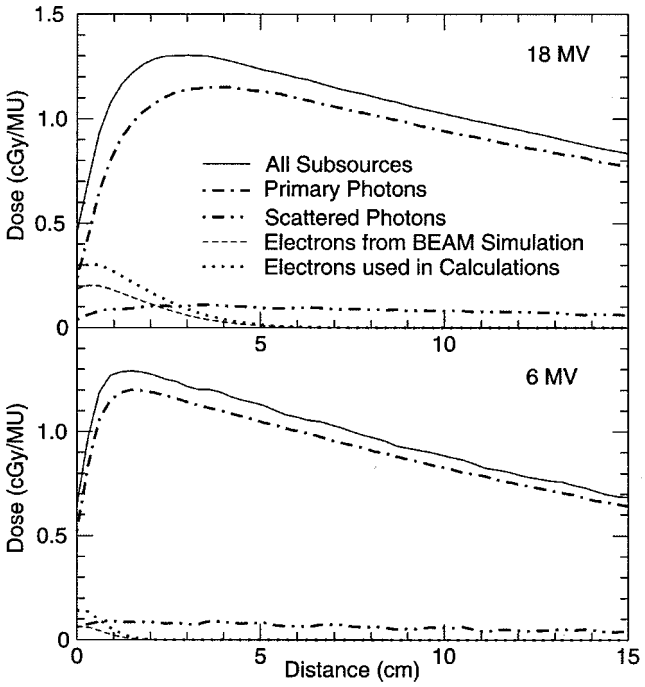

FIG. 4. Central-axis depth-dose distributions for $20\times20\,\mathrm{cm}^2$ 6 and 18 MV beams incident on a water phantom, positioned at 90 cm SSD. Most of the dose is contributed by primary photons. While electron subsource contributions in the buildup region are significant for the $20\times20\,\mathrm{cm}^2$ field (shown here), they are less than 2% for $10\times10\,\mathrm{cm}^2$ and smaller fields. The dotted line shows the effect of increasing the electron source weight on the electron component of the dose, to achieve a better fit to measurement.

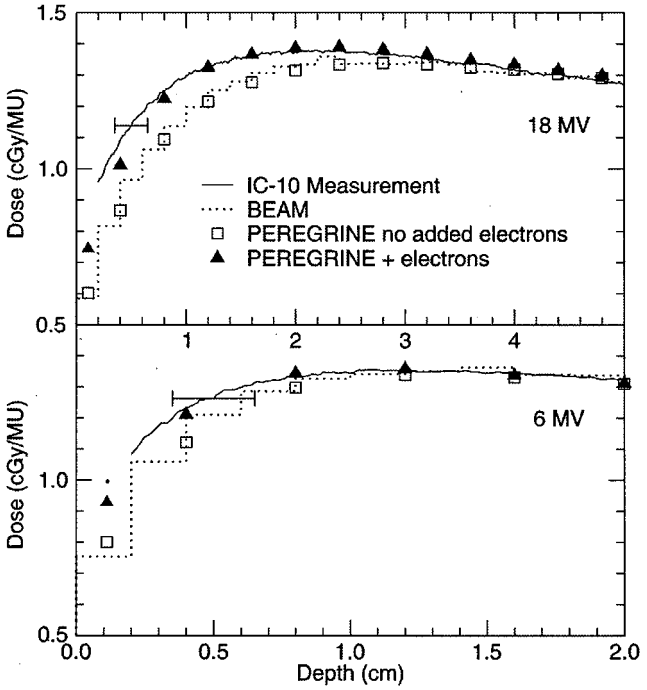

FIG. 5. Central-axis depth-dose distributions comparing PEREGRINE (with and without added electrons) and BEAM calculations with IC-10 ion chamber for depths in the buildup regions for a $38\times38\,\mathrm{cm}^2$ field at 90 cm SSD. Measurement error is shown at a single point. See Sec. II D. For this case, calculations have been normalized to measurements at a depth of 5 cm. BEAM and PEREGRINE (without added electrons) agree with each other, but predict a substantially smaller dose than measured with the ion chamber.

from the upper jaws, f_1, is characterized by a second-order polynomial fit to measurements made by varying the opening of the upper jaw while keeping the lower jaw fixed at 40 cm. Backscatter from the lower jaws is characterized by another second-order polynomial fit, f_2, to lower-jaw measurements made with the upper jaws open to 40 cm. The form of the correction is

$$\text{backscatter correction} = f_1(y)[(yf_2(x)/40) + 1 - y/40],$$

where x and y are the lower and upper jaw openings, respectively, and f_1 and f_2 are normalized such that $f_1(40) = f_2(40) = 1$. The backscatter correction depends only on the jaw openings and not on the individual jaw positions. This approximation is consistent with the backscatter calculations in Ref. 50 for a Varian 2100C at 10 MV. This reference finds that the off-axis location of the jaw opening does not have a significant effect on the magnitude of the backscatter. For cases of a $10\times10\,\mathrm{cm}^2$ field 5 cm off-axis and a $5\times5\,\mathrm{cm}^2$ field 10-cm off-axis, we find better than 1% agreement between our measurements and calculations (see Sec. III).

Finally, comparisons with large-field measurements reveal a deficit in dose calculations in the dose-buildup region for open fields, which exceeds experimental error, as discussed later. This effect, shown for a $38\times38\,\mathrm{cm}^2$ field in Fig. 5, is evident in depth-dose curves calculated with both BEAM and PEREGRINE. Measurements shown in Fig. 5 are described in Sec. II D. Each PEREGRINE calculation data point represents the center of a dosel. The surface dosel was positioned with its center at the water surface. Because energy deposited in air contributes a negligible portion of the total dose, we report the dose for the surface dosel at the correct effective depth. These simulations make use of the same phase space data from the BEAM simulation of the fixed components of the accelerator, upstream of the jaws. Results of BEAM and PEREGRINE agree within a statistical precision of less than 1% demonstrating that the discrepancy is not due to the beam model or radiation transport physics in PEREGRINE. The magnitude of the dose deficit near the surface increases with increasing field size, and goes away for fields blocked by wedges or trays. Based on this evidence, we hypothesize that it is caused by a source of electrons in the accelerator head that is not fully accounted for in the treatment head simulation with BEAM. To account for this, we increase the weight of the electron subsource by 120% and 50% for 6 and 18 MV beams, respectively. While the 6 MV discrepancy is smaller, it requires a greater proportion of added electron source, because a smaller number of the source electrons reach the central axis at 90 cm SSD for 6 MV than for 18 MV. Further investigation of the source of missing electrons is beyond the scope of this work.

C. Beam commissioning

The beam commissioning procedure consists of two parts: (1) selecting/interpolating the initial electron energy incident

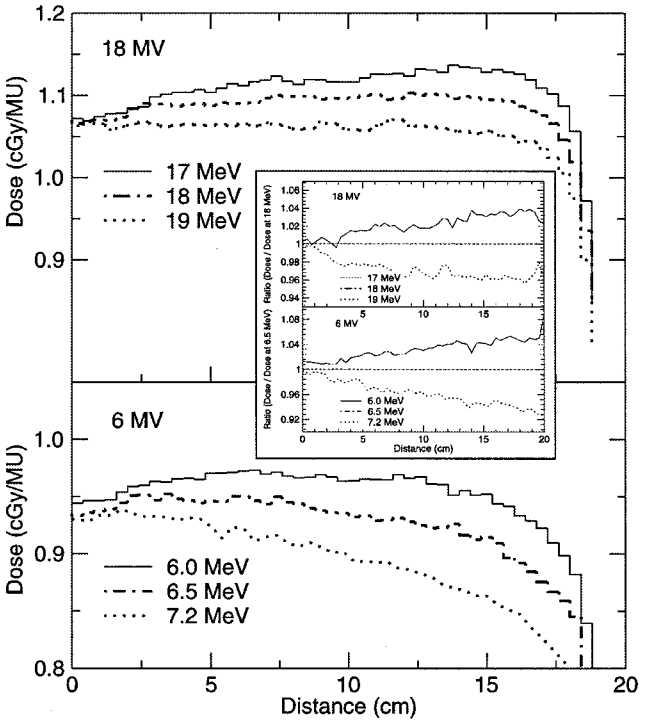

FIG. 6. Profiles at 10 cm depth for a $38\times38\ \text{cm}^2$ field incident on a water phantom at 90 cm SSD, showing the effect of varying the initial electron energy. The largest-field profile is most sensitive to initial electron energy. Profiles at 10 cm depth were chosen because of their insensitivity to the effects of contamination electrons. The inset shows ratios of the profiles with respect to the profile for the 18 and 6.5 MV profiles, respectively.

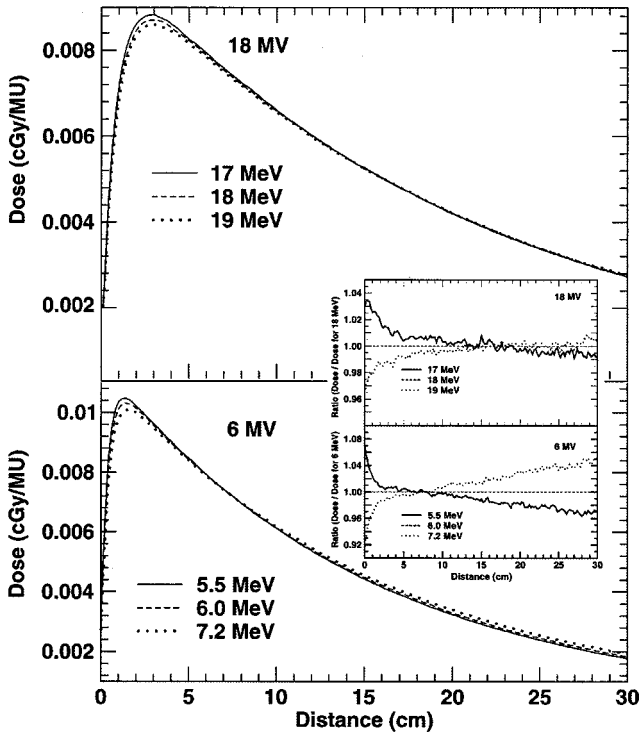

FIG. 7. Central-axis depth-dose curves for a $2\times2\ \text{cm}^2$ field incident on a water phantom at 90 cm SSD, showing the effect of varying the initial electron energy. The $2\times2\ \text{cm}^2$ field has the depth-dose curve that is the most sensitive to initial electron beam energy. The inset shows ratios of the profiles with respect to the profile for the 18 and 6.0 MV profiles, respectively.

on the bremsstrahlung target and (2) setting the dose per monitor unit, based on the specific calibration of the accelerator.

Field flatness is sensitive to beam energy.[19,25] Figures 6 and 7 show how the electron beam energy affects the field flatness and depth-dose for 38×38 and $2\times2\ \text{cm}^2$ fields, respectively. Calculation results were obtained by normalizing the calculated dose to measured dose at a depth of 10 cm on the central axis of a $10\times10\ \text{cm}^2$ field for each electron voltage used. The effect of electron beam energy on field flatness is most apparent for the largest field size. Figure 6 shows that a variation of 8% in the off-axis ratio (defined at 10 cm from the axis) at 10 cm depth results from change in electron beam energy from 6 to 7.2 MeV. A 5% off-axis ratio variation results from a 17 to 19 MeV change in electron beam. Small-field depth-dose curves are most sensitive to electron energy. Figure 7 shows that $2\times2\ \text{cm}^2$ depth-dose curves are most affected at shallower depths. Variation in electron beam energy from 5.5 to 7.2 MeV results in a relative difference of 8% at a depth of 30 cm. A variation of 17–19 MeV results in a maximum relative difference of less than 3% at a depth of 30 cm. Because large-field flatness is more sensitive than depth dose to electron energy for high energy x-ray beams and because profile measurements are less subject to systematic errors due to slight misalignment of the gantry and beam scanner, it is used to estimate the beam energy for this study. The use of profiles to determine beam energy relies on accurate modeling of the flattener. Therefore, it is important to check that depth-dose curves are calculated accurately as well.

BEAM simulations were completed, and the corresponding device files generated for a set of beam energies around the nominal energy of the machine. Using PEREGRINE, dose profiles were calculated for each of these energies. An interpolation was done between the calculated profiles to find the beam energy that matched the measured profile. This energy was then used to generate a new device file by doing a linear interpolation using the nearest two device files, without rerunning BEAM. For this study, voltages were linearly interpolated from a library of simulations at 6.0, 6.5, and 7.2 MeV and 17, 18, and 19 MeV for 6 and 18 MV beams, respectively. Voltages selected were 6.2 and 18.5 MeV for 6 and 18 MV beams.

Once the effective energy is determined, we calibrate the internal particle fluence metric in terms of dose per monitor unit (MU). The user inputs the cGy/MU at 10 cm depth on the central axis of a $10\times10\ \text{cm}^2$ field, and PEREGRINE uses this number to determine the effective weight of each history, so that dose is calculated in units of cGy/MU.

For purposes of simulations, the geometry of collimator jaws, wedges, wedge trays, block trays, and multileaf collimators (MLCs) are described in terms of density, composition, shape, and location. Block thickness, material, and density, and aperture shape and MLC leaf positions are

described by the user at calculation time. For the calculations shown in this paper, wedges are composed of stainless steel (density: 7.86 g/cm^3; composition: 0.5% Si, 18% Cr, 2.0% Mn, 69.9% Fe, 9.6% Ni by weight) and blocks are composed of cerrobend (density: 9.38 g/cm^3; composition: 6.0% Cd, 8.4% Sn, 29.6% Pb, 56.0% Bi by weight). All wedge dimension and position data were taken from measurements of the specific wedges. We shifted the 60° wedge by 2 mm in the lateral direction to obtain good agreement with measurements for wedge factors.

D. Measurements

All measurements in this paper were taken on the University of California San Francisco Varian Clinac 2100C using a Wellhofer water phantom. Output, profile, and depth dose measurements were made using a Wellhofer IC-10 ionization chamber (0.147 cm^3 active volume with a 6.0 mm diameter and 6.3 mm active length, 0.4 cm wall thickness). Small-field profile measurements were made with a Scanditronix photon diode (*p*-type silicon, chip thickness of 0.45 mm, 2.5 mm diameter).

Measurements are reported as dose per monitor unit. This was determined as follows. All measurements were normalized to a single reference measurement taken at 10 cm depth for a $10\times10\,\mathrm{cm}^2$ field at 90 cm SSD. A dose rate was assigned to measured current for the reference measurement according to dose expected at that point based on the calibration condition of the accelerator, 1 cGy/MU at 100 cm SSD for a $10\times10\,\mathrm{cm}^2$ field at a depth of $d_{\max}$.

We assign an overall experimental uncertainty of 1% in relative dose, 1.5 mm in depth relative to the surface for the IC-10 measurements and 1% in relative dose, 0.5 mm in depth for the diode measurements, as justified in the following. Profile data were shifted by up to 1 mm in the direction perpendicular to the beam axis to achieve the best match with calculation. This shift is well within accepted tolerance of jaw and MLC leaf positioning and uncertainty in the position of the ion chamber relative to the beam axis. The IC-10 was positioned in depth with an accuracy of 1.5 mm (2 standard deviations), combining an estimated 1.0 mm uncertainty in the position of the detector relative to the water surface with a 0.5–1.0 mm systematic uncertainty in the point of measurement correction. This correction, which was 1.8 mm at 6 MV and 2.0 mm at 18 MV, with the detector shifted upstream, is recommended by Wellhofer based on unpublished measurements and was automatically applied by Wellhofer software during scanning. Separate comparisons of IC-10, with this shift applied, and extrapolation ion chamber measurements were done of depth dose distributions in the build-up region at 100 cm SSD. IC-10 and extrapolation ion chamber measurements agreed within 1.5 mm at depths greater than 2.0 mm. Larger discrepancies than this were apparent within 2.5 mm of the surface, due to the finite diameter of the IC-10. Therefore, measurements are reported at depths greater than 2.0 mm. The precision on the IC-10 ion chamber measurements is $\pm0.3\%$. Systematic errors for relative dose measurements beyond the buildup region, including variations in water-to-air stopping power ratio with detector position, are not expected to exceed 1% for measurements we report using either ion chamber or diode measurements.[51,52]

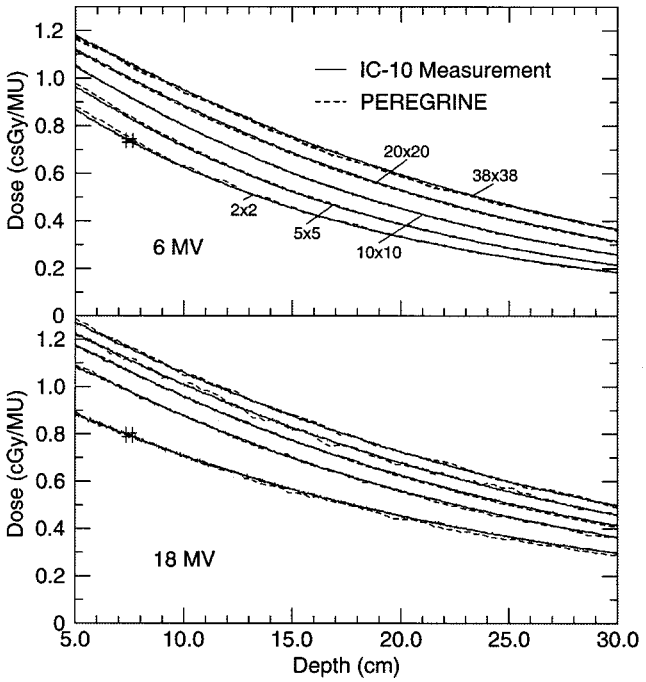

FIG. 8. Central axis depth-dose curves for 2×2, 5×5, 10×10, 20×20, and $38\times38\,\mathrm{cm}^2$ fields at 90 cm SSD. PEREGRINE calculations (dashed lines) are compared with IC-10 measurements. Measurement error is shown at a single point at 5 cm depth for the $2\times2\,\mathrm{cm}^2$ field.

For measurements with the multileaf collimator, photon diode measurements are used because of their superior spatial resolution. Measurements for 5×5, 10×10, and $20\times20\,\mathrm{cm}$ fields demonstrated good agreement between profile measurements with a diode and IC-10 ion chamber measurements in areas of low dose gradient. Diode profile measurements were normalized to an ion chamber depth dose measurement.

III. RESULTS

We compare calculations with measurements for open fields ranging from 2×2 to $38\times38\,\mathrm{cm}$, and for fields modified by wedges, blocks, and multileaf collimators. All comparisons are reported in dose per monitor unit, including a correction for the variation in backscatter to the monitor chamber with jaw opening, with no further normalization done. That is, depth dose curves and profiles reported include relative output and wedge factors. All measurements had a source-to-surface distance (SSD) of 90 cm. This distance is representative of typical patient setups.

In discussing the difference between calculated and measured dose at a given spatial point, we use two quantities: the difference relative to the measured dose at that point and the difference relative to the maximum measured dose. We refer

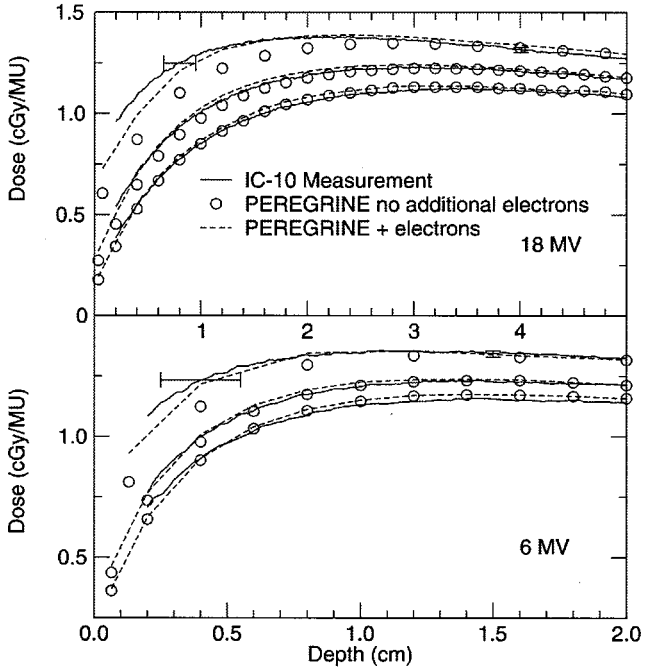

FIG. 9. Depth-dose curves in buildup region for 5×5, 10×10, and $38\times38\,\mathrm{cm}^2$ fields incident on a water phantom positioned at 90 cm SSD. PEREGRINE calculations are compared with IC-10 ion chamber measurements. Measurement errors are shown at single points for the $38\times38\,\mathrm{cm}^2$ field.

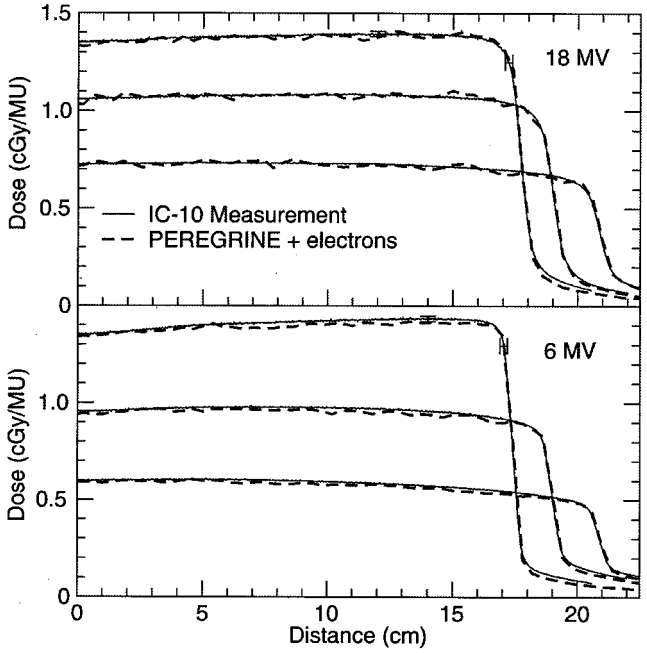

FIG. 10. Profiles at d_{max}, 10, and 20 cm depths for a $38\times38\,\mathrm{cm}^2$ fields incident on a water phantom positioned at 90 cm SSD. PEREGRINE calculations are compared with IC-10 ion chamber measurements. Measurement errors are shown at single points for the profile at d_{max}. Added electrons in the source make no significant difference to the profiles.

to these as local relative difference and the difference relative to maximum dose, respectively. The latter is likely to be of greater interest clinically.

Open field comparisons were done for both square and rectangular fields. Figure 8 shows measured and calculated depth-dose curves on the central axis of the beam, at depths greater than 5 cm, for 2×2, 5×5, 10×10, 20×20, and $38\times38\,\mathrm{cm}^2$ fields. Calculated depth-dose distributions are slightly steeper than for measurements, with a maximum local relative difference of 2%, evident for the $2\times2\,\mathrm{cm}^2$ 18 MV field. A possible explanation for this is that electron voltage, tuned by the procedure described previously, is slightly low. However, Fig. 10 shows better than 1% agreement between calculations and measurements for $38\times38\,\mathrm{cm}^2$ field profiles, which are also sensitive to beam energy.

Figure 9 compares measured and calculated depth-dose curves on the central axis of the beam near the phantom surface for 5×5, 10×10, and $38\times38\,\mathrm{cm}^2$ fields. In this figure the surface dosels were shifted in the same manner as was done for Fig. 5. Calculations in Fig. 5 were renormalized to measured dose at 5 cm. Calculations in Fig. 9 were not renormalized. With added electrons, calculations agree with measurements to within 2% and 8% (local relative difference at a depth of 4 mm), or 0.4 mm and 1.2 mm (isodose displacement), of the dose measurement for 6 and 18 MV, respectively. We have three pieces of evidence that support the presence of additional electrons upstream of the jaws: (1) field-size and energy dependence of the discrepancy, (2) excellent agreement between the calculated and measured

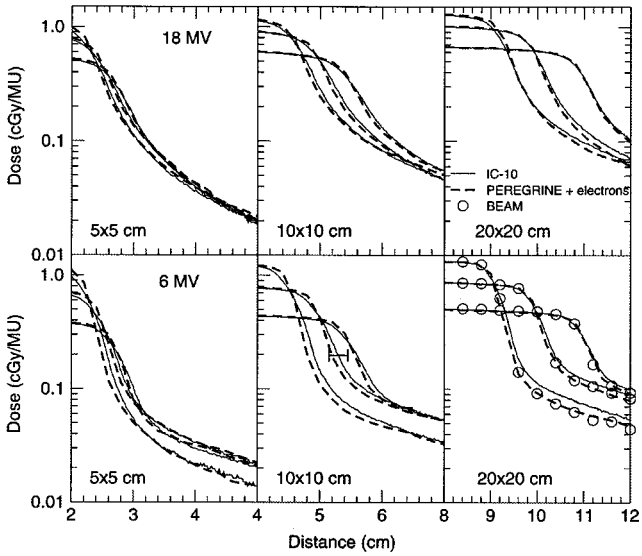

FIG. 11. Profiles at d_{max}, 10, and 20 cm depths for 5×5, 10×10, and $20\times20\,\mathrm{cm}^2$ fields incident on a water phantom positioned at 90 cm SSD. To emphasize comparisons outside the beam penumbra, results are shown on a semilog scale. PEREGRINE calculations are compared with IC-10 ion chamber measurements. Positional measurement error is shown at a single point on a 6 MV $10\times10\,\mathrm{cm}^2$ profile. For the field size showing the greatest discrepancy with measurements ($20\times20\,\mathrm{cm}^2$ field, 6 MV beam), we also compare with BEAM/DOSEXYZ calculations. PEREGRINE and BEAM calculations agree with each other, but predict a lower dose than measured. Added electrons in the source make no significant difference to the profiles.

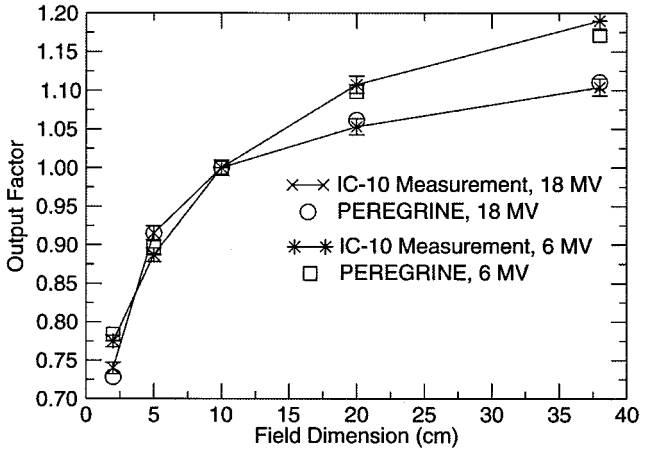

FIG. 12. Calculated and measured output factors at 10 cm depth for 2×2, 5×5, 10×10, 20×20, and $38\times38\,cm^2$ fields.

depth dose for large fields below wedges (discussed in the following), and (3) reduction of the discrepancy in the buildup for large fields in the presence of a 6 mm acrylic tray (data not shown). Increasing the weight of the electron subsource for both the 6 and 18 MV beam models provides close agreement in the buildup region wherever discrepancies occur, but small discrepancies can remain because increasing the weight is an approximation or because some residual discrepancies may be experimental.

Figures 10 and 11 show profiles for several representative fields. The $38\times38\,cm^2$ field comparison (Fig. 10) shows agreement to within a maximum local relative difference of 1% between calculations and measurements inside the field. Beam energies were chosen to achieve a good match for these measurements. In the penumbra region, the effects of the IC-10 chamber width cause up to 1 mm discrepancies with calculations for 6 MV. These effects are much smaller for 18 MV, because of its broader penumbra. Comparisons outside the field (Fig. 11) reveal that PEREGRINE agrees to within 2% with measurements for 5×5 and $10\times10\,cm^2$ fields. However, outside the $20\times20\,cm^2$ field, PEREGRINE underestimates the dose by as much as 10% of the measured dose. This has little clinical significance, as these errors are less than 1% of the dose on the central axis. Calculations done with BEAM/DOSXYZ show the same discrepancy, agreeing with PEREGRINE. Measurement/calculation differences may be due to a source of scattered or leakage radiation that is not currently being accounted for in the beam accelerator head simulation.

Figure 12 is a comparison between calculated and measured output factors on the central axis of the beam at a depth of 10 cm. PEREGRINE includes a provision to account for backscatter as described in Sec. II. With a backscatter correction, PEREGRINE agrees with measurements to within 1.2% and 1.6% for 2×2 and $38\times38\,cm^2$ fields, respectively. For 6 MV, the backscatter correction used in PEREGRINE (renormalized to 1 for a $10\times10\,cm^2$ field) results in factors of 0.994, 1.000, 1.025 for a 2×2, 10×10, and $38\times38\,cm^2$ fields, respectively. For 18 MV, the backscatter correction

TABLE I. Comparison between measured and calculated relative output factor (ROF)—output relative to a $10\times10\,cm^2$ field at 10 cm depth—for 6 and 18 MV beams.

Beam	Field size	Meas. ROF	Calc. ROF	Relative difference
6 MV	$5\times20\,cm^2$	0.960	0.972	1.3%
	$20\times5\,cm^2$	0.949	0.950	0.8%
	$5\times40\,cm^2$	0.984	0.983	0.1%
	$40\times5\,cm^2$	0.962	0.962	0.1%
	$10\times10\,cm^2$	1.028	1.026	0.2%
	5 cm off-axis			
	$5\times5\,cm^2$	0.922	0.923	0.1%
	10 cm off-axis			
18 MV	$5\times20\,cm^2$	0.977	0.981	0.4%
	$20\times5\,cm^2$	0.955	0.956	0.03%
	$5\times40\,cm^2$	0.994	0.984	0.9%
	$40\times5\,cm^2$	0.964	0.955	1%
	$10\times10\,cm^2$	1.011	1.020	0.9%
	5 cm off-axis			
	$5\times5\,cm^2$	0.940	0.949	0.95%
	10 cm off-axis			

results in factors of 0.990, 1.000, 1.043 for the same fields, respectively. PEREGRINE calculations include a backscatter correction for all figures in this paper, unless otherwise stated.

Comparisons between calculations and measurements for 5×20, 20×5, 5×40, and $40\times5\,cm^2$ rectangular fields and off-axis 5×5 and $10\times10\,cm^2$ square fields were also done in order to stress the backscatter correction factor and investigate the effects of added electrons. Table I summarizes mea-

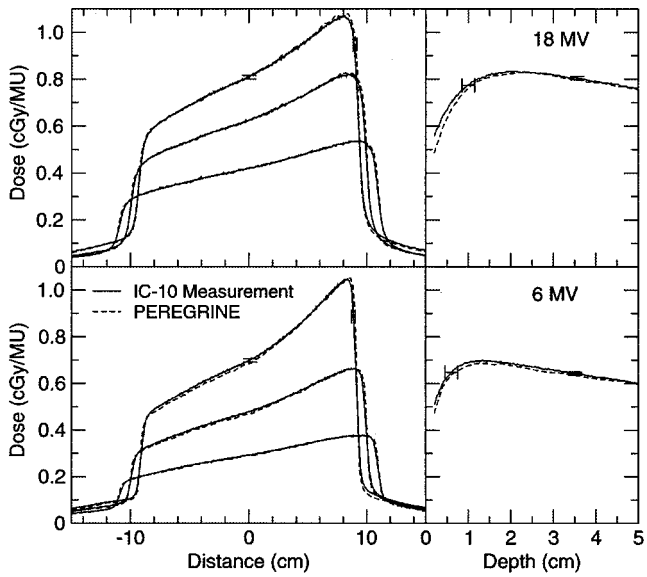

FIG. 13. Calculations and IC-10 measurement profiles at d_{max}, 10, and 20 cm depths for a 45° wedge, $40\times20\,cm^2$ field incident on a water phantom at 90 cm SSD. Measurement errors are shown at single points (on axis for dose uncertainty and 9 cm off axis for positional uncertainty for profiles at d_{max}; at depth for dose uncertainty and in the buildup region for positional uncertainty for depth-dose comparisons). Added electrons in the source makes no difference to dose distributions for wedges. No additional electron source has been added.

TABLE II. Comparison between measured and calculated wedge factors for 15°, 45°, and 60° wedges. Wedge factor (WF) is defined as dose at 10 cm depth with wedge in (20×40 cm^2 field for 15° and 45°, 15×40 cm^2 for 60°) divided by dose at 10 cm depth for a 10×10 cm^2 open field.

Beam	Wedge	Meas. WF	Calc. WF	Relative difference
6 MV	15°	0.916	0.912	0.4%
	45°	0.596	0.588	1%
	60°	0.497	0.492	1%
18 MV	15°	0.911	0.922	1%
	45°	0.652	0.648	0.6%
	60°	0.565	0.564	0.1%

sured and calculated output factors (relative to a 10×10 cm^2 field at 10 cm depth), which agree to within 1.3% with measurements. Depth-dose calculations (with added electrons) in the buildup region of the rectangular fields agree with measurements to within an isodose shift of less than 1 mm for each case. The added electrons have little effect in the buildup region, consistent with the small square field results. Depth dose calculations deeper than the maximum dose agree with measurements to within 2% and 1% local relative difference for 6 and 18 MV, respectively.

Figure 13 compares calculations with measurements for fields modified by a wedge. Profile calculations for a 20×40 cm^2 field modified by a 45° wedge agree with measurements to within 2% local relative difference inside the field. Both 6 and 18 MV show a slightly greater slope to the calculated profile than is measured. This probably relates to a small error in the specific composition or density used for the steel wedge. The 6 MV calculations slightly underestimate dose, while 18 MV calculations slightly overpredict dose, consistent with the same trends shown for open field output factors. Outside the beam, calculations agree with measurements to within 4% for the profiles at 10 and 20 cm depth. For the profile at $d_{\max}$, calculations underpredict the dose outside the beam by up to 9% local relative difference, consistent with our observations for open fields. This difference amounts to 1% of the dose on the central axis.

Calculated central axis depth-dose curves shown in Fig. 13 agree with measurement to within 2% for depths greater than $d_{\max}$ for both 6 and 18 MV beams. In the buildup region, calculations agree with measurements to within 7%, resulting in isodose displacement of less than 1 mm. This is similar to differences found in open-field buildup comparisons after an additional electron source has been added. No additional electrons need be added to the source to achieve this level of agreement, as the wedge absorbs most electrons from the source. The wedge itself introduces a new source of electrons, emanating from the bottom of the wedge tray. The small residual discrepancy in the buildup observed for wedged fields may be due to experimental uncertainty, such as chamber positioning and changes in chamber response at shallow depths.

Comparisons between calculations and measurements for 15° and 60° wedges (20×40 and 15×40 cm^2 fields, respectively) show similar results, with maximum local relative difference of 2% inside the beam at depths greater than $d_{\max}$, for both 6 and 18 MV, and 7% in the buildup region. Table II summarizes measured and calculated wedge factors (defined as dose at 10 cm with wedge relative to dose at 10 cm for a 10×10 cm^2 open field) for all wedges studied.

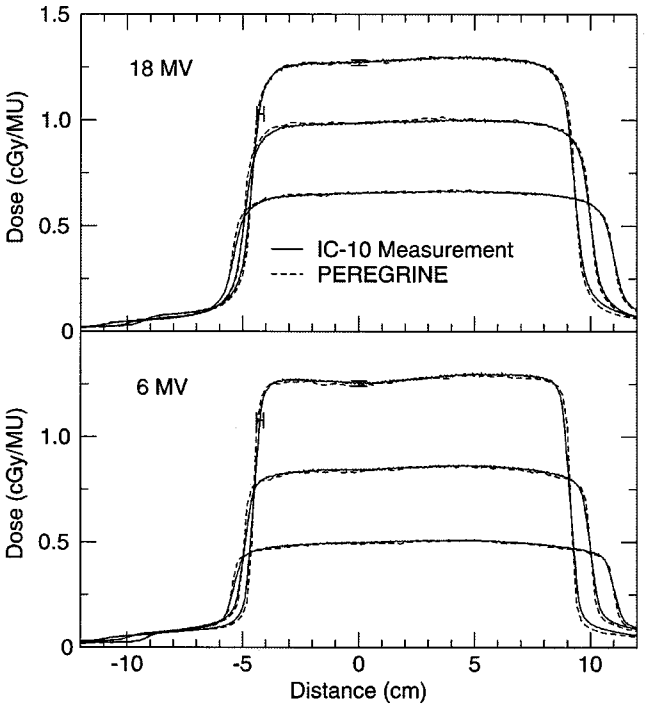

FIG. 14. Calculations and IC-10 measurement profiles at $d_{\max}$, 10, and 20 cm depths for a cerrobend block on an acrylic tray modifying a 20×20 cm^2 field incident on a water phantom positioned at 90 cm SSD. Measurement errors are shown at single points (on axis for dose uncertainty and 4 cm off axis for positional uncertainty for the profile at $d_{\max}$). Added electrons in the source make no significant difference to the calculated dose distributions for blocks/block trays. No additional electron source has been added.

Calculations shown in Fig. 14 are for a 7.5-cm-thick cerrobend quarter-beam block fixed on top of a 0.6-cm-thick acrylic block tray. Results agree with ion chamber measurements to within less than 1% local relative difference at 6 MV and less than 2% at 18 MV in unblocked areas, and less than 3% (0.2% of the maximum dose) for 6 and 18 MV in blocked areas. Calculated dose outside the penumbra agrees with measurements to better than 6% local relative difference (0.5% of the maximum dose) on the unblocked side and better than 3% (0.1% of the maximum dose) on the blocked side.

A complex comb pattern, with blocked and open regions, was used to compare PEREGRINE calculations to photon diode measurements for the multileaf collimator (Fig. 15). Collimator jaws were set to 20×26 cm^2. On the side of the beam close to the 5-cm-wide open region, the beam is collimated by two leaves, which extend 2 cm beyond the collimator jaw, which is set to the edge of the multileaf collimator. Leakage radiation scattering around the collimator jaw and multileaf collimator is responsible for the small peak at the edge of the

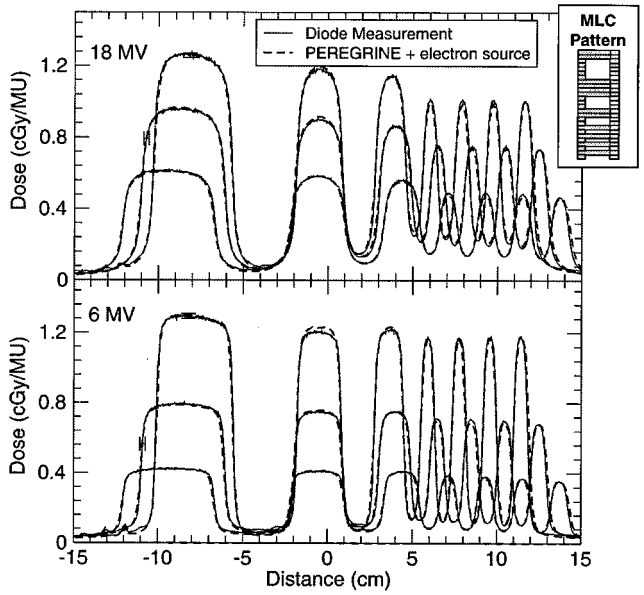

FIG. 15. Calculations and photon diode measurement profiles at d_{max}, 10, and 20 cm depths for a multileaf collimator modifying a 20×26 cm^2 field incident on a water phantom positioned at 90 cm SSD. Diode profile measurements were normalized to an ion chamber depth-dose measurement. Measurement errors are shown at single points (8 cm off axis for dose uncertainty and 11 cm off axis for positional uncertainty) for the profile at d_{max}. The inset shows the MLC pattern. Added electrons make no significant difference to the profiles.

field. On the 1 cm side of the comb pattern, only the collimator jaw blocks the field. Because of the large number of high-dose-gradient areas, we compare measurements with photon diode measurements. Agreement between calculations and measurements is generally $<2\%$ of maximum dose for low-gradient areas of both unblocked and MLC-blocked areas. Comparisons of profiles measured with a diode and an IC-10 ion chamber indicate that, in the low dose-gradient regions of this plot, the diode agrees with the ion chamber to within 1% of the maximum dose.

IV. SUMMARY AND CONCLUSIONS

In this paper, we provide an overview of the PEREGRINE code system, including descriptions of the current radiation transport physics, x-ray beam model, and commissioning procedure. The results of a set of calculation/measurement comparisons show the accuracy of the overall implementation of the code, including the beam model and commissioning procedure. The only normalization done was to use a single-point calibration. Results, summarized in Table III, indicate good agreement between calculations and measurements in dose per monitor unit for distributions under open fields and for a variety of beam modifiers. In the low-dose gradient regions inside the field, utilizing a published correction curve for monitor chamber backscatter and an empirical correction to the electron source fluence, PEREGRINE agrees with measurements to within 2% of the dose at the measurement point. Calculated output factors and wedge factors are good to within 2%. In the penumbra region, PEREGRINE predictions result in spatial isodose discrepancies of less than 1 mm. Outside the penumbra, discrepancies are larger: PEREGRINE systematically predicts a lower dose than measured, with relative discrepancies as high as 15%. While these differences are large compared to the dose at the measurement point, they amount to less than 1% discrepancies expressed as a fraction of the maximum dose at that depth.

Where tested (open fields) PEREGRINE agrees with EGS4 (BEAM/DOSEXYZ), with both codes underpredicting dose in the buildup region of large fields and in the area blocked by the collimator jaws. This, combined with the systematic nature of the discrepancies, suggest that the remaining discrep-

TABLE III. Summary of maximum discrepancies observed in calculation/measurement comparisons.

Relative output factor	Added electrons	Results		
$2\times2-38\times38$ cm^2 square fields	No effect	1.6% with backscatter correction; 3% (6 MV) and 5% (18 MV) if backscatter correction not applied		
5×20, 20×5, 5×40, 40×5 cm^2 rectangular fields	No effect	1.3% with backscatter correction		
5×5 cm^2 field 10 cm off axis, 10×10 cm^2 field 5 cm off-axis	No effect	1% with backscatter correction		
Depth dose	**Added electrons**	**Depth: $<d_{max}$ (buildup)**		**Depth: $>d_{max}$[a]**
$2\times2-38\times38$ cm^2 square fields	Results without	3 mm (6 MV) 5 mm (18 MV)		2%
	Results with	1 mm (6 and 18 MV)		2%
5×20, 20×5, 5×40, 40×5 cm^2 rectangular fields	Results without	2 mm		2%
	Results with	1 mm		2%
15°, 45°, and 60° wedges	No effect	1 mm		2%
Profiles (depths=d_{max},10,20 cm)	**Added electrons**	**Inside field[b]**	**Penumbra**	**Outside field[b]**
38×38 cm^2	No effect	1%	1 mm	1%
2×2, 5×5, 10×10, 20×20 cm^2	No effect	2%	1 mm	1%
15°, 45° and 60° wedges	No effect	2%	1 mm	1%
Cerrobend quarter-beam block	No effect	2%	1 mm	0.5%
Multileaf collimator	No effect	2%	1 mm	1%

[a]Local relative difference.
[b]Difference relative to maximum dose at that depth.

ancies are caused by leakage or scatter radiation not accounted for in the treatment head simulation.

With the added electron source and backscatter correction, the dose calculation is accurate to either 2% of maximum dose or 1.2 mm in isodose position. This accuracy applies over the wide field size range considered and for standard beam modifiers, including wedges, blocks, and multileaf collimators.

ACKNOWLEDGMENTS

The authors gratefully acknowledge the contributions of W. P. Chandler, L. J. Cox, M.-A. Descalle, R. Fortner, D. Fujino, R. Hill, D. Jong, S. H. May, E. I. Moses, R. W. Patterson, C. Powell, and A. E. Schach von Wittenau for their important contributions to the PEREGRINE effort. Without their vision, management, and technical contributions, this work would not have been possible. We would also like to thank the U.S. Department of Energy Office of Biological and Environmental Research, Medical Sciences Division for their support. This work was performed under the auspices of the U.S. Department of Energy by the Lawrence Livermore National Laboratory under Contract No. W-7405-ENG-48.

[a]Electronic mail: chs@llnl.gov

[1] K. R. Shortt, C. K. Ross, A. F. Bielajew, and D. W. O. Rogers, "Electron beam dose distributions near standard inhomogeneities," Phys. Med. Biol. **31**, 235–249 (1986).

[2] *Monte Carlo Transport of Electrons and Photons*, edited by T. M. Jenkins, W. R. Nelson, A. Rindi, A. E. Nahum, and D. W. O. Rogers (Plenum, New York, 1988).

[3] T. R. Mackie, "Applications of the Monte Carlo method in radiotherapy," *Dosimetry of Ionizing Radiation Vol. 3*, edited by K. Kase, B. Bjarngard, and F. H. Attix (Academic, New York, 1990), pp. 541–620.

[4] P. Andreo, "Monte Carlo techniques in medical radiation physics," Phys. Med. Biol. **26**, 861–920 (1991).

[5] R. Mohan, "Why Monte Carlo?," in *Proceedings of the XIIth International Conference on the Use of Computers in Radiation Therapy*, Salt Lake City, UT, edited by D. D. Leavitt and G. Starkschall (Medical Physics Publishing, Madison, WI, 1997), pp. 16–18.

[6] J. J. DeMarco, T. D. Solberg, and J. B. Smathers, "A CT-based Monte Carlo simulation tool for dosimetry planning and analysis," Med. Phys. **25**, 1–11 (1998).

[7] M. R. Arnfield, C. Hartmann Siantar, J. Siebers, P. Garmon, L. Cox, and R. Mohan, "The impact of electron transport on the accuracy of computed dose," Med. Phys. **27**, 1266–1274 (2000).

[8] L. Wang, C-S. Chui, and M. Lovelock, "A patient-specific Monte Carlo dose-calculation method for photon beams," Med. Phys. **25**, 867–878 (1998).

[9] H. Neuenschwander, T. R. Mackie, and P. J. Reckwerdt, "MMC—a high-performance Monte Carlo code for electron beam treatment planning," Phys. Med. Biol. **40**, 543–574 (1995).

[10] P. J. Keall and P. W. Hoban, "Super-Monte Carlo: A 3D electron beam dose calculation algorithm," Med. Phys. **23**, 2023–2034 (1996).

[11] C. L. Hartmann Siantar *et al.*, "Lawrence Livermore National Laboratory's PEREGRINE Project," in Ref. 5, pp. 19–22.

[12] M. Fippel, "Fast Monte Carlo dose calculation for photon beams based on the VMC electron algorithm," Med. Phys. **26**, 1466–1475 (1999).

[13] J. Sempau, S. J. Wilderman, and A. F. Bielajew, "DPM, a fast, accurate Monte Carlo code optimized for photon and electron radiotherapy treatment planning dose calculations," Phys. Med. Biol. **45**, 2263–2291 (2000).

[14] C.-M. Ma, J. S. Li, T. Pawlicki, S. B. Jiang, and J. Deng, "MCDOSE—A Monte Carlo dose calculation tool for radiation therapy treatment planning," *XIIIth International Conference on the Use of Computers in Radiation Therapy* (Springer, New York, 2000).

[15] I. Kawrakow and M. Fippel, "Investigation of variance reduction techniques for Monte Carlo photon dose calculations using XVMC," Phys. Med. Biol. **45**, 2163–2183 (2000).

[16] R. Mohan, C. Chui, and L. Lidofsky, "Energy and angular distributions of photons from medical linear accelerators," Med. Phys. **12**, 592–597 (1985).

[17] J. V. Siebers, P. J. Keall, B. Libby, and R. Mohan, "Comparison of EGS4 and MCNP4B Monte Carlo codes for generation of photon phase space distributions for a Varian 2100C," Phys. Med. Biol. **44**, 3009–3026 (1999).

[18] D. W. O. Rogers, B. A. Faddegon, G. X. Ding, C-M. Ma, J. We, and T. R. Mackie, "BEAM: A Monte Carlo code to simulate radiotherapy treatment units," Med. Phys. **22**, 503–524 (1995).

[19] D. M. J. Lovelock, C. S. Chui, and R. Mohan, "A Monte Carlo model of photon beams used in radiation therapy," Med. Phys. **22**, 1387–1394 (1995).

[20] G. Küster, T. Bortfeld, and W. Schlegel, "Monte Carlo simulations of radiation beams from radiotherapy units and beam limiting devices using the program GEANT," in Ref. 5, pp. 150–152.

[21] B. Faddegon, J. Balogh, R. Mackenzie, and D. Scora, "Clinical considerations of Monte Carlo for electron radiotherapy treatment planning," Radiat. Phys. Chem. **53**, 217–227 (1998).

[22] C.-M. Ma and S. B. Jiang, "Monte Carlo modeling of electron beams from medical accelerators," Phys. Med. Biol. **44**, R157–R189 (1999).

[23] A. E. Schach von Wittenau, L. J. Cox, P. M. Bergstrom, W. P. Chandler, C. L. Hartmann Siantar, and R. Mohan, "Correlated histogram representation of Monte Carlo derived medical accelerator photon-output phase space," Med. Phys. **26**, 1196–1211 (1999).

[24] J. Deng, S. B. Jiang, A. Kapur, J. Li, T. Pawlicki, and C-M. Ma, "Photon beam characterization and modeling for Monte Carlo treatment planning," Phys. Med. Biol. **45**, 411–427 (2000).

[25] B. A. Faddegon, P. O'Brien, and D. L. D. Mason, "The flatness of Siemens linear accelerator x-ray fields," Med. Phys. **26**, 220–228 (1999).

[26] C.-M. Ma, B. A. Faddegon, D. W. O. Rogers, and T. R. Mackie, "Accurate characterization of Monte Carlo calculated electron beams for radiotherapy," Med. Phys. **24**, 401 (1997).

[27] D. E. Cullen, M. H. Chen, J. H. Hubbell, S. T. Perkins, E. F. Plechaty, J. A. Rathkopf, and J. H. Scofield, Lawrence Livermore National Laboratory Report UCRL-50400, Volume 6, LLNL, Livermore, 1989.

[28] J. H. Hubbell, W. J. Veigele, E. A. Briggs, R. T. Brown, D. T. Cromer, and R. J. Howerton, J. Phys. Chem. Ref. Data **4**, 471 (1975).

[29] C. M. Davisson and R. D. Evans, Rev. Mod. Phys. **24**, 79 (1952).

[30] J. H. Hubbell, H. A. Gimm, and I. Overbo, J. Phys. Chem. Ref. Data **9**, 1023 (1980).

[31] "International Commission on Radiation Units and Measurements (ICRU)," ICRU Report No. 37, ICRU, Bethesda, 1984.

[32] F. H. Attix, *Introduction to Radiological Physics and Radiation Dosimetry* (Wiley, New York, 1986).

[33] W. R. Nelson, H. Hirayama, and D. W. O. Rogers, "The EGS4 Code System," Report No. SLAC—265, Stanford Linear Accelerator Center, Stanford, CA, 1985.

[34] A. F. Bielajew and D. W. O. Rogers, "Effects of a Møller cross section error on the EGS4 code," Med. Phys. **23**, 1153 (1996).

[35] S. T. Perkins, D. E. Cullen, and S. M. Seltzer, Lawrence Livermore National Laboratory Report No. UCRL-50400, Vol. 31, LLNL, Livermore, 1991.

[36] A. F. Bielajew, R. Mohan, and C. Chui, "Improved bremsstrahlung photon angular sampling in the EGS4 code system," National Research Council of Canada Report No. PIRS-0203, 1989.

[37] B. A. Faddegon, C. K. Ross, and D. W. O. Rogers, "Angular distribution of bremsstrahlung from 15-MeV electrons incident on thick targets of Be, Al, and Pb," Med. Phys. **18**, 727–739 (1991).

[38] I. Lux and L. Koblinger, *Monte Carlo Particle Transport Methods: Neutron and Photon Calculations* (CRC Press, Boca Raton, 1991), p. 40.

[39] M. J. Berger, *Monte Carlo Calculation of the Penetration and Diffusion of Fast Charged Particles*, in Methods in Computational Physics Vol. 1 (Academic, New York, 1963), p. 135.

[40] G.-Z. Moliére, "Theorie der Streuung schneller geladener Teilchen. I. Einzelstreuung am abgeschirmten Coulomb-Field," Z. Naturforsch. A **2A**, 133–145 (1947).

[41] J. Barò, J. Sempau, J. M. Fernàndez-Varea, and F. Salvat, "PENELOPE: An algorithm for Monte Carlo simulation of the penetration and energy loss

of electrons and positrons in matter,'' Nucl. Instrum. Methods Phys. Res. B **100**, 31–46 (1995).
[42] I. Kawrakow and A. Bielajew, ''On the condensed history technique for electron transport,'' Nucl. Instrum. Methods Phys. Res. B **142**, 253–280 (1998).
[43] H. W. Lewis, ''Multiple scattering in an infinite medium,'' Phys. Rev. **78**, 526–529 (1950).
[44] A. F. Bielajew, D. W. O. Rogers, and A. E. Nahum, ''Monte Carlo simulation of ion chamber response to ^{60}Co—Resolution of anomalies associated with interfaces,'' Phys. Med. Biol. **30**, 419–428 (1985).
[45] A. E. Schach von Wittenau, P. M. Bergstrom, Jr., and L. J. Cox, ''Patient-dependent beam-modifier physics in Monte Carlo photon dose calculations,'' Med. Phys. **27**, 935–947 (2000).
[46] S. M. Ross, *Simulation*, 2nd ed. (Academic, San Diego, 1997), p. 116.
[47] A. F. Bielajew and D. W. O. Rogers, ''PRESTA: The parameter reduced electron-step transport algorithm for electron Monte Carlo transport,'' Nucl. Instrum. Methods Phys. Res. B **18**, 165–181 (1987).
[48] K. L. Lam, M. S. Muthuswamy, and R. K. Ten Haken, ''Measurement of backscatter to the monitor chamber of medical accelerators using target charge,'' Med. Phys. **25**, 334–338 (1998).
[49] C. Dunzenli, B. McClean, and C. Field, ''Backscatter into the beam monitor chamber: Implications for dosimetry of asymmetric collimators,'' Med. Phys. **20**, 363–367 (1993).
[50] H. H. Liu, T. R. Mackie, E. C. McCullough, ''Modeling photon output caused by backscattered radiation into the monitor chamber from collimator jaws using a Monte Carlo technique,'' Med. Phys. **27**, 737–744 (2000).
[51] D. Sheikh-Bagheri, D. W. O. Rogers, C. K. Ross, and J. P. Seuntjens, ''Comparison of measured and Monte Carlo calculated dose distributions from the NRC linac,'' Med. Phys. **27**, 2256–2266 (2000).
[52] M. Westermark, J. Arndt, B. Nilsson, and A. Brahme, ''Comparative dosimetry in narrow high-energy photon beams,'' Phys. Med. Biol. **45**, 685–702 (2000).